PEM fuel cell membrane hydration measurement by neutron imaging

D.J. Ludlow [a], C.M. Calebrese [b], S.H. Yu [c], C.S. Dannehy [d], D.L. Jacobson [e],
D.S. Hussey [e], M. Arif [e], M.K. Jensen [a,*], G.A. Eisman [b]

[a] *Department of Mechanical Aerospace and Nuclear Engineering, JEC 2049, Rensselaer Polytechnic Institute, 110 8th Street, Troy, NY 12180, USA*
[b] *Department of Materials Science and Engineering, Rensselaer Polytechnic Institute, Troy, NY 12180, USA*
[c] *Department of Chemistry, Rensselaer Polytechnic Institute, Troy, NY 12180, USA*
[d] *Plug Power, Latham, NY 12110, USA*
[e] *National Institute of Standards and Technology, Gaithersburg, MD 20899, USA*

Abstract

Neutron scattering experiments on a proton exchange membrane fuel cell were performed to assess the ability to quantify water in the membrane and electrode/gas diffusion layers. Previous studies have shown that liquid water is easily resolved within flow channels, making neutron imaging a valuable tool in the design and analysis for water management in fuel cells. This study demonstrates the resolution of water content changes within the membrane electrode assembly and membrane alone. These preliminary results extend the use of neutron imaging as a more complete water dynamics measurement tool including membrane hydration.
© 2006 Elsevier B.V. All rights reserved.

Keywords: Fuel cell; Water distribution; Membrane hydration; Neutron imaging; Proton exchange membrane

1. Introduction

Fuel cells have the potential to shift the way we generate energy to a more efficient and environmentally friendly manner. They avoid production of undesirable by-products by directly converting chemical energy to electrical and thermal energy. However, while fuel cells provide significant promise there is still much work needed to bring these devices into everyday and widespread use.

One of the most common types of fuel cells is the low-temperature proton exchange membrane (PEM) fuel cell. One significant problem in this type of fuel cell is water management. As the name implies, PEM fuel cells rely on a separating proton conducting membrane as the electrolyte. The commonly used membrane today, a perfluorosulfonic acid-based polymer (PFSA), has a Teflon®-like [1] backbone and side-chains terminating with sulfonic acid sites (HSO$_3$). When the membrane is hydrated, it is believed that hydrogen ions (protons, H$^+$) are solvated with varying amounts of water molecules; furthermore, the sulfonic acid sites are hydrated [2]. The hydration level is critical as it dictates all the properties of the membrane. From a transport perspective, the water content of the membrane and the resultant solvated protons facilitate proton conduction. The proton transport can be achieved by a number of mechanisms, all water-based. If the membrane is not fully hydrated not all of the sulfonic acid sites may be utilized, thus resulting in a lower concentration density of proton carriers in the membrane and a drop in proton conductivity. In addition to proton conductivity, the mechanical properties of the membrane are a function of water content [3]. For example, in the DuPont Nafion® series of membranes (1100 E.W. series), mechanical properties decrease with increasing water content, and gas permeability and proton conductivity increase. Water content in the fully saturated Nafion® membrane (1100 E.W. series) is approximately 20–30 wt%; hence, hydration has a significant impact on structure/property relationships. In some cases tensile forces, resulting from membrane hydration fluctuations, can create catastrophic failures. Lastly, as hydration levels are reduced, the membrane becomes more susceptible to chemical attack. This degradation mechanism has been proposed to be related to peroxide attack on the membrane and ionomer in the electrodes [4].
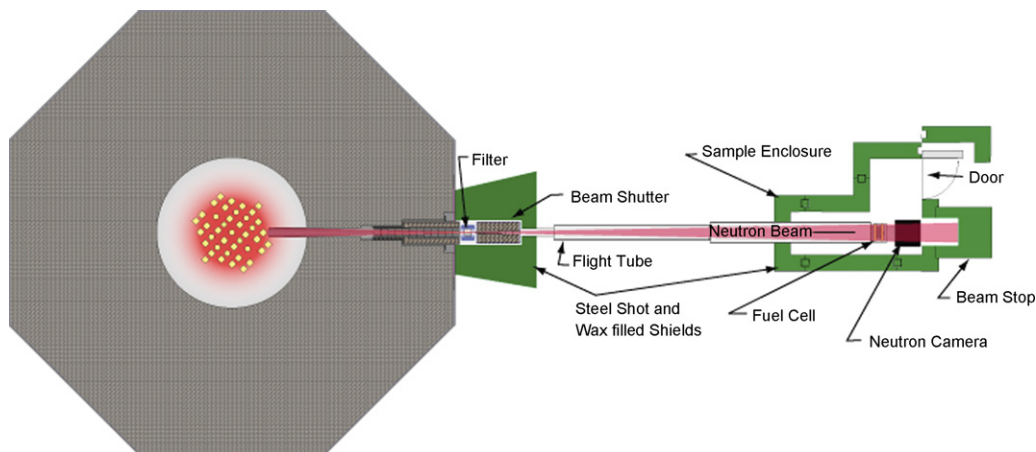

Fig. 1. NCNR BT-6 (beam tube 6) imaging facility.

The membrane is not the only component affected by water content. The electrodes are also at risk; too little water can reduce conductivity in proton conducting layers within the electrode layer, and too much water can flood the electrode, thereby reducing the effective active area of the catalyst. Such water issues result in life limiting failure mechanisms in the cell. Even gas supply channels can be affected by water. Gas composition in the cathode flow channels changes as oxygen is consumed and water is produced. The gas dew point may eventually rise to the operating temperature of the cell, leading to condensation and water blockage of the gas diffusion layer (GDL) and flow channels.

With hydration having such a strong influence on PFSA-based PEM fuel cell performance, water management is key to reaching optimal performance, reliability, and lifetimes. To minimize water management problems fuel cell developers have moved to thinner membranes, hydrophilic electrodes, and plate treatments which facilitate water movement within the flow field channels. Likewise, there are a number of operating parameters which can be controlled to obtain desired hydration levels. Reactant gas stream humidification levels and temperature, cell temperature, and current density all can be controlled to help maintain proper cell hydration. However, the situation is complex; all these parameters are coupled, and control of any one parameter affects the others. In addition, even though system inputs may be controlled, non-uniformities exist within an individual cell and among cells of a stack.

Management of such a complex system must be considered during the design process, and researchers must have an understanding of the water dynamics within the system. This understanding is usually developed by a combination of modeling and experimentation. Since the late 1980s [5] many models have been proposed to predict the performance of PEM fuel cells [6] with some specifically targeting water management [7]. A major difficulty lies with the experimental aspect. Typical model validation consists of comparing numerically and experimentally obtained polarization curves, with little or no local data available to compare performance variations across the cell. Distributed measurements of water, temperature, and current would be useful for the confirmation of theory and to improve the design process. Methods to gather experimental data in a non-invasive, non-destructive process are in need, and some possible technologies are not necessarily directly applicable to fuel cells. If an X-ray like device to monitor the water in a fuel cell could be utilized, especially in an operating cell, the insight gained would be invaluable.

Distributed current measurements have been performed by a number of research groups [8–18]; most of these studies have utilized flow fields segmented into discrete current collectors. Each individual collector is monitored for voltage and current. Other methods include segmented electrodes and segmented membrane and electrode assemblies (MEA) [10]. Distributed temperature measurements have been made using arrays of thermocouples [19,20] and infrared imaging [21,22]. Water has been detected through the use of neutron imaging [23–25], magnetic resonance imaging (MRI) [26], micro-Raman spectroscopy [27], gas chromatography [28,29], and visible light [22]. One experiment consisted of neutron imaging to detect multi-phase conditions within direct methanol fuel cells (DMFC) [30]. Ideally, a distributed measurement technique would cover a large field of view with high spatial, depth, and time resolution, could be implemented without significant modifications to a typical cell, and could be used while the cell is operating. Each of the above techniques meets at least one of these guidelines, but few meet all of them.

The application of neutron imaging to fuel cells provides X-ray like distributed water measurements and has begun to yield valuable information and insight into water dynamics in the flow fields that sandwich the membrane. Neutrons bombarding the target are scattered with varying effectiveness by the materials in the beam path. In particular, hydrogen is very effective at scattering neutrons, while other materials (e.g., aluminum, carbon, etc.) are not. Satija et al. [24] presented an excellent depiction of relative neutron scattering cross sections of various elements. The high hydrogen density of liquid water allows it to scatter neutrons quite well. Despite this recent application of neutron radiography to fuel cells, little has been reported in the open literature on the behavior of the water in the membrane or GDL.

In this paper, we report the results of neutron imaging experiments on a cell built with Gore[TM] 5510 membrane. This work

was initiated to understand the capabilities of neutron imaging as applied to fuel cells. The objective was to further refine the experimental methods and techniques used to analyze data. Preliminary data are presented that illustrate some capabilities of the technique.

2. Experimental technique and neutron scattering theory

2.1. Neutron imaging

The facility at the National Institute of Standards and Technology (NIST) Center for Neutron Research (NCNR) (Fig. 1) uses a heavy water reactor as the neutron source. The neutron beam is processed through collimators, filters, an aperture, and an evacuated flight tube. The aperture selector allows for 1 and 2 cm apertures. The 2 cm aperture (used in the present experiments) provides a flux rate of about $1.84 \times 10^7 \, \mathrm{cm^{-2} \, s^{-1}}$ with an approximate *L/D* ratio of 280 [31].

The neutrons pass through the target and bombard a scintillating screen. Each collision with the screen triggers a nuclear reaction which emits visible light. Images of the illuminated scintillating screen are captured with a Varian Paxscan 2520 amorphous silicon detector. The detector is placed directly in the beam path behind the scintillating screen and is capable of frame rates as high as 30 frames per second [31]. The detector has a pixel pitch of 127 μm, but the system resolution is limited to ∼200 μm through the conversion of neutrons to visible light by the scintillating screen.

The fuel cell is mounted on a motor controlled sample manipulation stage capable of 2 axis horizontal motion, as well as pitch, roll, and yaw rotations. System resolution is maximized by placing the fuel cell and detector as close to the scintillating screen as possible (see Fig. 2).

The raw image intensity represents the light intensity emitted from the scintillating screen. Bright areas represent high neutron fluxes and dark areas low. Areas of high hydrogen concentration create a neutron shadow, showing up as a dark region in the image. While raw images can be viewed immediately after capture (Fig. 3), image processing is required to obtain quantitative data. Hence, processed images are obtained by performing a series of data reduction steps.
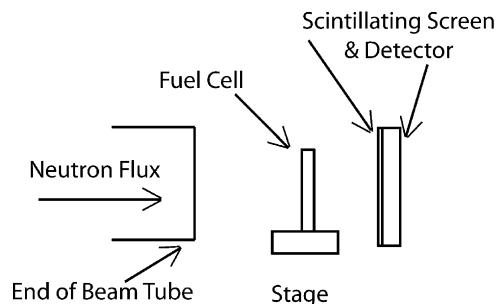

Fig. 2. Layout of fuel cell and detector. Fuel cell is shown oriented normal to the beam, resulting in images of the cell face. Parallel orientation results in a cross section view as reported by Bellows et al. [23].
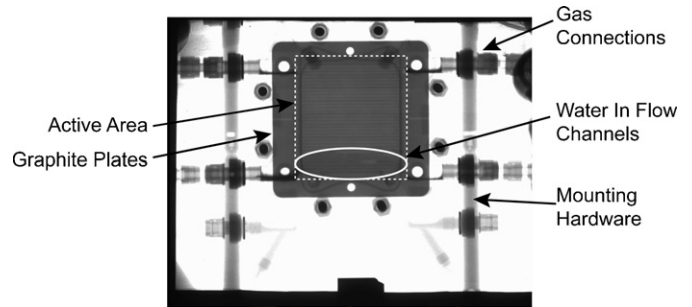

Fig. 3. Raw image of cell. Image was taken prior to any gas flow and operation. The MEA is located in the square region in the upper middle portion of the image. The outer portions of the image contain mounting hardware, inlet, exhaust, coolant, and load connections.

Eq. (1) shows the relationship between the neutron beam and attenuation due to materials in the neutron flight path.

$$I = I_o \exp \left(-\sum_i \mu_i t_i \right) \tag{1}$$

I represents the neutron beam flux rate at the scintillating screen and I_o is the uninterrupted neutron beam flux upstream of the target. The exponent accounts for scattering due to all materials, *i*, within the beam path; μ is the attenuation length, and *t* is the total thickness of that element in the beam path. The attenuation length is found experimentally (by calibration) and represents the scale by which the species scatters neutrons per unit thickness.

The exponent contains a sum consisting of the μt products for all materials in the beam path (e.g., water, aluminum end plates, plumbing, etc.). Division of an image of a hydrated fuel cell by an image of a dehydrated fuel cell results in subtraction of the exponents and isolation of the change in water content. The order of image processing steps is as follows:

(1) Capture images of the fuel cell at an operating point of interest.
(2) Capture images of the dehydrated fuel cell.
(3) Average images in each image set to reduce noise. Averaging images reduces noise by the square root of the number of images used. Large image sets (hundreds to thousands) are desired for noise reduction.
(4) Isolate scattering due to water by dividing the averaged cell image by the averaged dry cell image.

$$\frac{I}{I_{\mathrm{drycell}}} = \exp(-\mu_{\mathrm{water}} t_{\mathrm{water}}) \tag{2}$$

The resulting image contains the difference between the original image and the dry cell image.

(5) Take the negative natural log of the result of step 4 to obtain an image of the μt product of water.

$$D = -\ln \left(\frac{I}{I_{\mathrm{drycell}}} \right) = \mu_{\mathrm{water}} t_{\mathrm{water}} \tag{3}$$

(6) Find the change in water thickness by dividing D by the attenuation length of water.

$$t_{water} = \frac{D}{\mu_{water}} = -\frac{\ln(I/I_{dry\ cell})}{\mu_{water}} \qquad (4)$$

Spatial non-uniformity in flux across the beam thickness is assumed to be constant over time and is removed during step 4 as a by-product of image division. If non-comparative images were desired, a "flat-field" image (no target in beam path) would be used to normalize the image for non-uniformity across the beam thickness. In addition to the beam flux being non-uniform through the cross section, the flux can vary with time. The beam flux time variance can be removed by normalizing with reference to a static portion of the image. The average value for the selected static region is monitored and the entire image intensity is scaled appropriately to maintain the average intensity of selected region constant over time.

2.2. Fuel cell

A 50 cm² fuel cell was built with graphite single channel flow fields (both anode and cathode) and aluminum end plates. The MEA was built with Gore™ 5510 membrane and electrodes consisting of polytetraflouroethylene (PTFE) impregnated SGL CARBON AG diffusion media with carbon supported platinum catalyst. The cell was configured with coolant chambers on each side of the MEA–plate assembly for temperature control. Pre-operation of as-received (dry) MEAs consisted of operation with fully humidified gases at 70 °C and 0.4 V until performance stabilized. The cell architecture was such that the membrane extended outside the active area and was sealed between the flow field plates by Teflon® gaskets surrounding the active region (Fig. 5B). As explained later, this architecture allowed for comparison of water within the MEA and membrane alone.

During operation, the cell was supplied with humidified hydrogen and air through a fuel cell test station. The station humidified dry gases using sparging bottles. Electric load was provided by a programmable load bank in tandem with the test station. Cell temperature was controlled by pumping water through channels on the back side of the graphite plates. Heavy water was used to avoid excessive neutron scattering by the cooling water, as deuterium does not scatter neutrons to the same degree as hydrogen.

The dehydrated cell state was obtained after all fuel cell operational experiments were completed, as there was the potential of damaging the cell with extreme dehydration. Dry gases were passed through the cell for 2 h with no load. A 1000-image set was captured after reaching the dehydrated state. The cell was then disassembled and the MEA removed from the cell. The MEA alone was weighed and placed in an 80 °C oven for 9 h and then weighed again. The purpose of weighing and drying the MEA was to measure any remaining water in the dehydrated cell in order to refine absolute water thickness measurements. Unfortunately, it was later found that experimental complications would not allow for absolute water measurements forcing the alternative analysis detailed below.
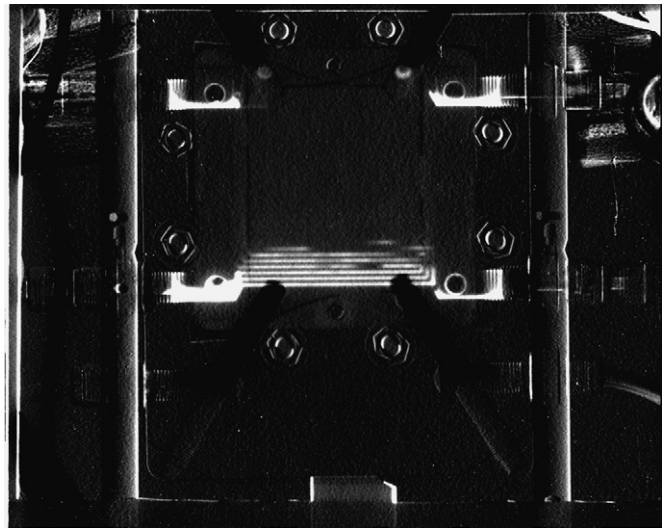

Fig. 4. The image in Fig. 3 processed such that only water remains. Liquid water is easily seen in the lower flow channels and manifolds. High intensity indicates thicker water regions.

3. Analysis

Original calculations produced unusually high water thicknesses, so much so that the membrane and GDL could not possibly contain such amounts. It was later discovered that there could in fact be some variation in water content within the carbon plates contributing to measurement error. For this reason, the analysis detailed below is performed using images taken immediately after the 20 min drying period as the "dry" image in the comparative analysis. The end result are data revealing the change in water content during the drying period, not absolute water content measurements. While the process described previously of measuring remaining water within the MEA would help refine absolute measurements, the technique does not apply to the following analysis.

Initial gas flow through the cell resulted in a dramatic change in water content. This was an effect of the cell being sealed immediately after hydration, trapping liquid water in the flow channels. As reported in previous literature, liquid water is quite easily observed in the flow channels after image processing steps [23–25,30]. However, liquid water is only slightly visible in the raw image (Fig. 3) in the lower channels of the plates.

Fig. 3 shows the raw image with liquid water residing in the lower flow channels. This image was taken prior to any operation or gas flow. Liquid water is only visible in the raw image with careful inspection and shows up as a washed out region. Fig. 4 contains a processed image in which high intensity indicates thicker regions of water. Note that image processing results in an image "negative" effect on water thickness.

Fig. 4 can be further processed to focus on the active region by cropping the image and applying a color mapping (Fig. 5A). The color mapping helps show changes in water content not easily resolved in gray scale images by the human eye. The color spectrum is such that blue coincides with thicker layers of water and orange thinner. In order to easily view changes in membrane water content, scaling has resulted in color saturation of liquid
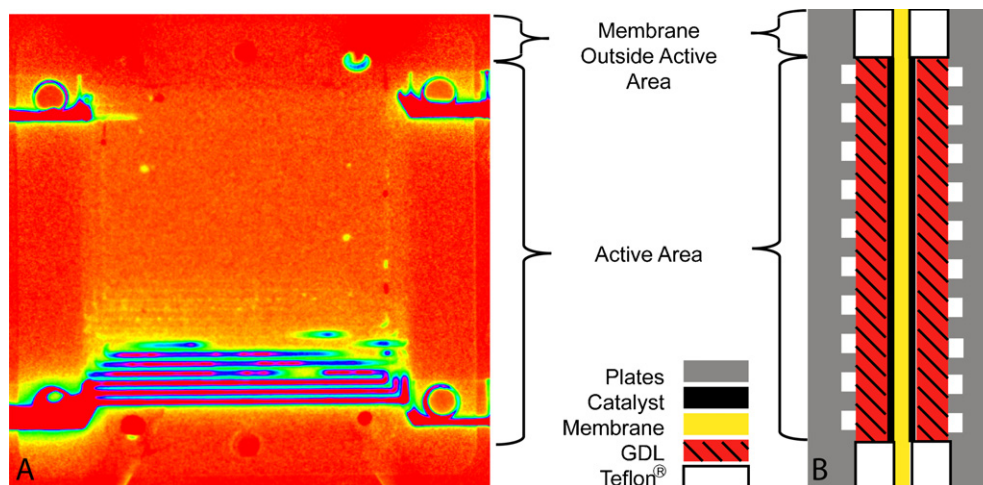
Fig. 5. Pre purge processed image of the cell (A). Further processing of the raw image (Fig. 3) was performed by cropping and applying a color map for ease of recognition. A linear HSV color mapping was applied with thresholds of 0 and 0.07. Water within and surrounding the holes at corners is located in the intake and exhaust ports. (B) A cross section of the cell, and shows the active area (membrane, GDL, electrode, and flow channels) and inactive outer region (only membrane sealed with Teflon® gaskets).

water in the channels. The very thick sections of water in the flow channels and manifolds show up as solid red. Color mapped images are only used to enhance qualitative analysis and, thus, any color saturation does not affect quantitative analysis.

Just as in Fig. 4, Fig. 5A shows the fuel cell prior to any gas flow or operation. In this case liquid water is not only visible in the flow channels, but there are faint indications of water thickness variations across the entire cell. Fig. 5B is a schematic of the cross section of the cell. Only the active area is surrounded by GDL and flow channels. The outer area is surrounded by Teflon® gaskets, and the only path for water loss is through the membrane plane.

Fig. 6A shows the cell immediately after purging of liquid water within the flow channels using a burst of dry nitrogen gas. There is a significant difference in water content, in comparison to Fig. 5A, in the flow channels and manifolds.

Images for Fig. 6B were captured after dry nitrogen gas was passed through the cell for 20 min. The change in water content

from the beginning (Fig. 6A) to the end (Fig. 6B) of the drying period is seen as the change in color from yellow to orange/red. Faintly visible is a change in the outer portion of the image, indicating a change in membrane hydration.

In comparing the previous three images, a change in the water content in the MEA region can be seen. The transition from Fig. 5A to Fig. 6A shows the obvious loss of liquid water in the flow channels. Less obvious, but still noticeable, is the change in water content from Fig. 6A to 6B. This change is not the result of simple purging of the flow channels, but is the loss of water from the MEA itself. Of further interest is the fact that the outer edges of these images contain membrane outside of the active area and under Teflon® gaskets. There is an observable change in intensity under the gaskets, indicating changes in membrane hydration via lateral transport of water through the membrane.

Further processing of images taken during the dry-out period showed a steady loss of water. A time series of reduced noise images was obtained by averaging images taken during dry-out
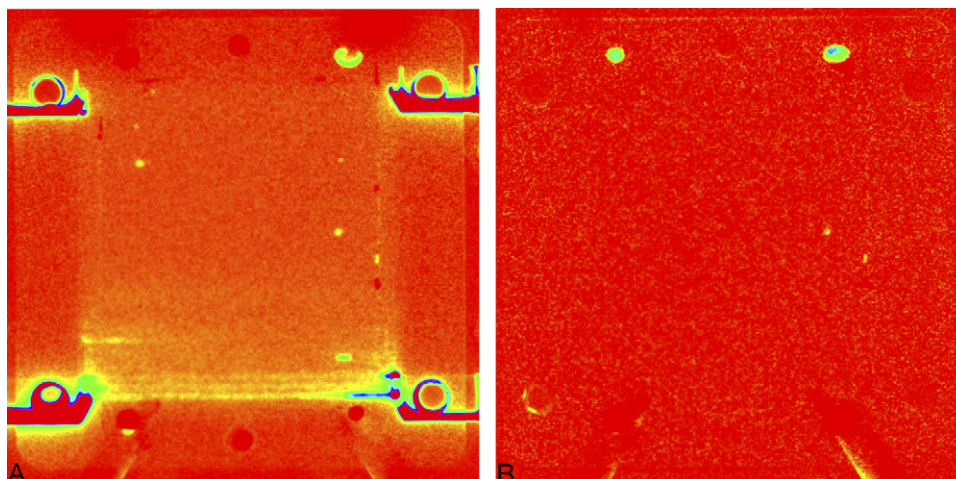

Fig. 6. Processed image from cell (A) after a burst of dry N_2 to purge water from the flow channels. (B) An image of the cell after 20 min of drying with dry N_2. The difference in color (yellow to orange/red), when comparing A to B, shows the loss of water within the MEA.
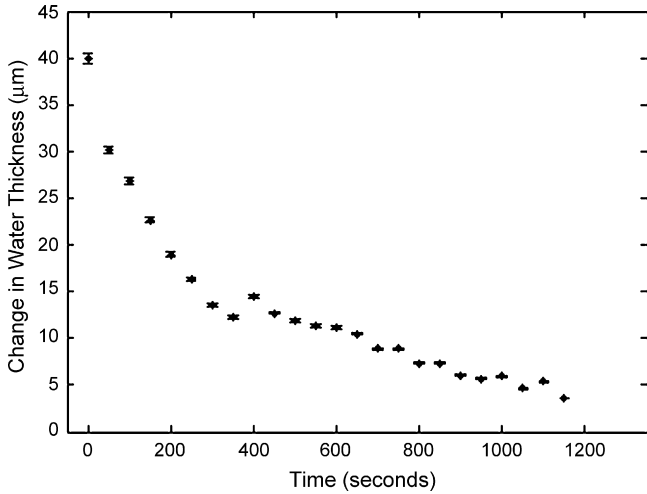
Fig. 7. Change in average active area water thickness. Series starts after the pre and post-purge images of Figs. 5 and 8. Error bars on each data point indicate uncertainty.

Fig. 9. Water thickness for the last image in the drying series is ~3.5 μm.

into non-overlapping 200 image blocks. The time series images were used to produce a movie showing the water loss in the cell over the 20 min period. The active region of the MEA was then averaged for each image in the series.

Fig. 7 shows the decay of average water thickness of the active area. (The cause of the inconsistency in the water thickness around the time of 400 s not clear.) Calculations indicated thicknesses of tens of micrometers. While these thicknesses are high for the membrane alone (roughly 25 μm thick when dehydrated and not having the capability to consume an equal thickness of water), it is not high for the combined membrane and GDL. The unusual trend in uncertainty (higher with larger water thickness and lower with thin sections) is due to the non-homogeneous water thickness across the averaged area. Variability in water thickness across the averaged active area is higher early in the drying period (as shown in Figs. 5 and 6A) and decreases as the bulk water contained in the flow channels and GDL is removed. These early variations in water thickness led to high variability and high levels of uncertainty in the averages calculated for
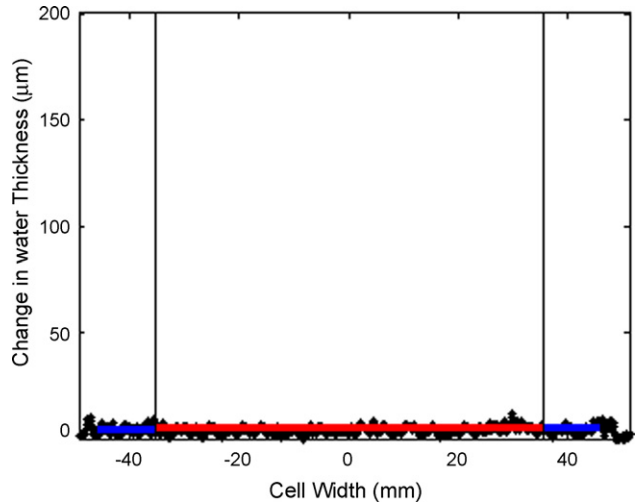
Fig. 7, but are not an indication of the capability of the measurement tool itself. The propagation of uncertainty was calculated following standard methods [32] using sample set standard deviations, Eq. (4), and the uncertainty found during calibration measurements of the attenuation length of water. The large number (at least 200 images in over a ~550 × 550 pixel area) of data points plays an integral roll in reducing uncertainty. Counting statistics support these low levels of uncertainty (Fig. 7), again by averaging together many images and many pixels within each image.

Measurements in the inactive outer region were compared to that of the active area and plotted for each image of the time series (Fig. 8). Figs. 8 and 9 were produced through the averaging of 1000 images for each figure, and the averaging of each column of pixels across of the cell width bounded by the upper and lower gas ports. Counting statistics indicate that the number of data points used to produce Figs. 8 and 9 should support uncertainties slightly below 1.5 μm. Improved uncertainty could be obtained by increasing the number of images within each data set.
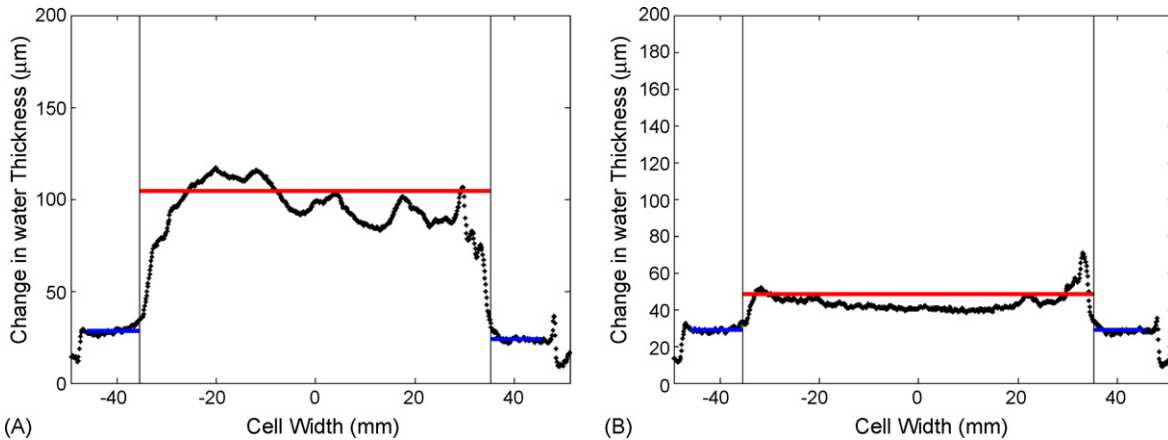

Fig. 8. Pre-purge (A) and post-purge (B) water loss thickness measurements. Red lines (center region) indicate the averages over the active area consisting of membrane and GDL. Blue lines (outer region) indicate the average of the membrane outside the active area. Vertical lines show the edge of the active area. Data points are averages over the height of the active area positions across the cell width.

The large difference in water content between the active (inner) and inactive (outer) regions of the pre-purge image are likely due to water in the flow channels and some saturation of the GDL. The post-purge image indicates the contributions due to water within the active region of the MEA that could not be easily removed with the quick purge.

After purging, the MEA continued to dry out over the 20 min period. Fig. 9 shows water measurements for the last image in the series. The drop in water content in the outer regions of the cell indicates measurable water loss in the membrane alone. The variability in Fig. 9 may be due non-homogeneous water thickness across the averaged areas for each data point. Comparing Fig. 9 to Fig. 8 shows the overall water loss during the drying period.

A follow-up experiment was performed in an attempt to quantify hydration changes within the plates. A single plate was hydrated in an 80 °C water bath for 20 min. The plate was weighed and placed in a 90 °C oven and then weighed at various time intervals. The plate lost an average of 0.7 μm of water over the initial 20 min period within the oven. Considering that there are two plates within the cell, this would indicate the potential for a total 1.4 μm water loss. In comparison, water loss in the outer regions of the membrane was found to be roughly 25 μm during the initial cell drying experiments. The capability of the membrane to take up approximately 30% water by weight (~8 μm) plus a 1.4 μm total average plate loss during follow-up experiments does not account for the full 25 μm loss in outer regions. This could indicate that the follow-up experiments did not accurately represent conditions during neutron imaging experiments, or that there are other potential sources of water variation within the field of view which must be accounted for during future experiments.

4. Conclusions

Experimental and theoretical considerations for the application of neutron imaging to water measurement in fuel cells have been presented. The use of neutron imaging appears to be useful beyond the previously shown capability to detect liquid water in flow channels. While there are uncertainties in the absolute measurements, the trend in the data does illustrate the ability to resolve variations in water content within the membrane and gas diffusion layers. Follow-up experiments indicated that carbon plate hydration is a factor and must be considered during experimentation. While it was found that the carbon plates do contribute to changes in water content, this does not invalidate conclusions regarding the capabilities of this technique to resolve small changes in water content. Future experiments will include non-porous plates, thus eliminating plate hydration contributions.

The ability to resolve changes in water content within the membrane of a PFSA based PEM fuel cell leads to the potential for a variety of future experiments with a shift in focus from liquid water in flow channels to membrane hydration studies. The potential exists for studies, for example, involving back diffusion of water from cathode to anode, forward diffusion from anode to cathode, exchange rate of water within the membrane, and electrode water affinity. Exchange rate measurements can be performed by utilizing heavy water and deuterium gas in various combinations with water and hydrogen gas, because deuterium does not have the same scattering characteristics as hydrogen and, thus, the two can be differentiated in neutron scattering experiments.

Acknowledgements

References

[1] Certain trade names and company products are mentioned in the text or identified in an illustration in order to adequately specify the experimental procedure and equipment used. In no case does such identification imply recommendation or endorsement by the National Institute of Standards and Technology, nor does it imply that the products are necessarily the best available for the purpose.

[2] J. Larminie, A. Dicks, Fuel Cell Systems Explained, second ed., Wiley, West Sussex, 2003, p. 70.

[3] G.A. Eisman, The application of Dow Chemical's perfluorinated membranes in proton exchange membrane fuel cells, J. Power Sources 29 (3–4) (1990) 389–398.

[4] R. Baldwin, M. Pham, A. Leonida, J. McElroy, T. Nalette, Hydrogen–oxygen proton–exchange membrane fuel cells and electrolyzers, in: NASA Conference Publication 3056: Space Electrochemical Research and Technology (SERT), 1989, pp. 127–134.

[5] D.M. Bernardi, M.W. Verbrugge, Mathematical model of a gas diffusion electrolyte bonded to a polymer electrolyte, AIChE J. 37 (8) (1991) 1151–1163.

[6] D. Cheddie, N. Munroe, Review and comparison of approaches to proton exchange membrane fuel cell modeling, J. Power Sources (2005).

[7] T.V. Nguyen, R.E. White, A water and heat management model for proton-exchange-membrane fuel cells, J. Electrochem. Soc. 140 (1993) 2178–2186.

[8] M. Naponen, T. Mennola, M. Mikkola, T. Hottinen, P. Lund, Measurement of current distribution in a free-breathing PEMFC, J. Power Sources 106 (2002) 304–312.

[9] S.J.C. Cleghorn, C.R. Deroun, M.S. Wilson, S. Gottesfeld, A printed circuit board approach to measuring current distribution in a fuel cell, J. Appl. Electrochem. 28 (1998) 663–672.

[10] J. Stumper, S.A. Campbell, D.P. Wilkinson, M.C. Johnson, M. Davis, In-situ methods for the determination of current distributions in PEM fuel cells, Electrochem. Acta 43 (1998) 3773–3783.

[11] K.H. Hauer, R. Potthast, T. Wuster, D. Stolten, Magnetotomography—a new method for analyzing fuel cell performance and quality, J. Power Sources 143 (2005) 67–74.

[12] C. Wieser, A. Helmbold, E. Gulzow, A new technique for two-dimensional current distribution measurements in electrochemical cells, J. Appl. Electrochem. 30 (2000) 803–807.

[13] Y.G. Yoon, W.Y. Lee, T.H. Yang, G.G. Park, C.S. Kim, Current distribution in a single cell of PEMFC, J. Power Sources 118 (2003) 193–199.

[14] N. Rajalakshmi, M. Raja, K.S. Dhathathreyan, Evaluation of current distribution in a proton exchange membrane fuel cell by segmented cell approach, J. Power Sources 112 (2002) 331–336.

[15] G. Bender, M.S. Wilson, T.A. Zawodzinski, Further refinements in the segmented cell approach to diagnosing performance in polymer electrolyte fuel cells, J. Power Sources 123 (2003) 163–171.

[16] A. Hakenjos, K. Tuber, L.O. Schumacher, C. Hebling, Characterizing PEM fuel cell performance using a current distribution measurement in comparison with a CFD model, Fuel Cells 4 (2004) 185–189.

[17] M. Noponen, J. Ihonen, A. Lundblad, G. Lindbergh, Current distribution measurements in a PEFC with net flow geometry, J. Appl. Electrochem. 34 (2004) 255–262.

[18] M.M. Mench, C.Y. Wang, M. Ishikawa, In-situ current distribution measurements in polymer electrolyte fuel cells, J. Electrochem. Soc. 150 (2003) A1052–A1059.

[19] M. Adzic, M.V. Heiter, D. Santos, Design of dedicated instrumentation for temperature distribution measurements in solid oxide fuel cells, J. Appl. Electrochem. 27 (1997) 1355–1361.

[20] M. Mench, D.J. Burford, T.W. Davis, In-situ temperature distribution measurement in an operating polymer electrolyte fuel cell, in: Proceedings of IMECE'03, 2003 ASME International Mechanical Engineering Congress & Exposition, Washington, DC, November 16–21, 2003.

[21] P. Millet, Water electrolysis using EME technology: temperature profile inside a Nafion membrane during electrolysis, Electrochem. Acta 36 (1991) 263–267.

[22] A. Hakenjos, H. Muenter, U. Wittstadt, C. Hebling, A PEM fuel cell for combined measurement of current and temperature distribution, and flow field flooding, J. Power Sources 131 (2004) 213–216.

[23] R.J. Bellows, M.Y. Lin, M. Arif, A.K. Thompson, D. Jacobson, Neutron imaging technique for in-situ measurement of water transport gradients within Nafion in polymer electrolyte fuel cells, J. Electrochem. Soc. 146 (1999) 1099–1103.

[24] R. Satija, D.L. Jacobson, M. Arif, S.A. Werner, In-situ neutron imaging technique for evaluation of water management systems in operating PEM fuel cells, J. Power Sources 129 (2004) 238–245.

[25] N. Pekula, K. Heller, P.A. Chuang, A. Turhan, M.M. Mench, J.S. Brenzier, K. Unlu, Study of water distribution and transport in a polymer electrolyte fuel cell using neutron imaging, Nucl. Instrum. Methods Phys. Res. A 542 (2005) 134–141.

[26] K.W. Feindel, L.P.A. LaRocque, D. Starke, S.H. Bergens, R.E. Wasylishen, In-situ observations of water production and distribution in an operating H_2/O_2 PEM fuel cell assembly using ^{1}H NMR microscopy, J. Am. Chem. Soc. 126 (2004) 11436–11437.

[27] H. Matic, A. Lundblad, G. Lindbergh, P. Jacobson, In-situ micro-Raman on the membrane in a working PEM cell, Electrochem. Solid-State Lett. 8 (2005) A5–A7.

[28] M.M. Mench, Q.L. Dong, C.Y. Wang, In-situ water distribution measurements in a polymer electrolyte fuel cell, J. Power Sources 124 (2003) 90–98.

[29] Q. Dong, J. Kull, M.M. Mench, Real-time water distribution in a polymer electrolyte fuel cell, J. Power Sources 139 (2005) 106–114.

[30] D. Kramer, E. Lehmann, G. Frei, P. Vontobel, A. Wokaun, G.G. Scherer, An on-line study of fuel cell behavior by thermal neutrons, Nucl. Instrum. Methods Phys. Res. A 542 (2005) 52–60.

[31] D.S. Hussey, D.L. Jacobson, M. Arif, P.R. Huffman, R.E. Williams, J.C. Cook, New neutron imaging facility at the NIST, Nucl. Instrum. Methods Phys. Res. A 542 (2005) 9–15.

[32] H.W. Coleman, W.G. Steele Jr., Experimentation and Uncertainty Analysis for Engineers, John Wiley & Sons, New York, 1989.